Computation of the elastodynamic response of finite doubly periodic cylinders by the wave finite element method

D. Duhamel

Computation of the elastodynamic response of finite doubly periodic cylinders by the wave finite element method

D. Duhamel[a,*]

[a]*Ecole Nationale des Ponts et Chaussées, Laboratoire Navier, ENPC/UGE/CNRS, 6 et 8 Avenue Blaise Pascal, Cité Descartes, Champs-sur-Marne, 77455 Marne La Vallée Cedex 2, France*

Abstract

Periodic media are widely studied for their industrial applications and unique ability to block wave propagation within certain frequency bands. For one-dimensional periodic systems, the Wave Finite Element (WFE) method efficiently computes dispersion relations and dynamic responses. Research on two-dimensional periodic structures extended this approach to periodicity along two directions, using finite element and reduction techniques such as Craig–Bampton and Bloch mode projection, including cases with damping and anisotropy. Beyond planar geometries, curved and helical periodic structures have been modeled with WFE and semi-analytical finite element methods to capture complex cyclic or screw symmetries for computing dispersion relations. Cylindrical configurations have also been explored, from simple vibration studies to wave propagation in layered or ribbed cylinders and metamaterial shells mainly for dispersion analysis or studies of infinite structures. As real structures are bounded, the present work focuses on finite elastic cylinders with double periodicity, using WFE to compute their dynamic response. Based on finite element matrices of a substructure, circumferential wavenumbers are imposed to obtain axial modes and responses as linear combination of modes. Numerical examples illustrate the method's effectiveness for modeling finite, doubly periodic cylindrical systems such as homogeneous structures, structures with holes and finally structures with resonators. The low computing time of the present approach allows the consideration of structures with a large number of substructures.

Keywords: doubly periodic structures, wave finite element, cylinder, linear elasticity, finite domain.

1. Introduction

Periodic media have attracted considerable attention in the past due to their widespread use in industry, their ease of manufacture, and their remarkable physical properties. One of their most important characteristics is the ability to stop wave propagation at frequencies within forbidden bands. The most common cases concern one-dimensional periodic media (periodic in one direction), for which the wave finite element (WFE) method, as described in [1–10] constitutes a good numerical tool for calculating the dispersion curves and the response of these structures to external excitations.

For two-dimensional periodic structures, meaning periodic along two directions, the first studies were carried out, for example, by [11, 12], who investigated wave propagation in order to calculate dispersion relations using finite element models. More recently, [13] studied two-dimensional wave propagation in periodic beam arrays, primarily to calculate dispersion curves, bandwidths and stopping bands. Wave propagation in more general two-dimensional periodic structures was studied by [14], who used the wave finite element method to calculate dispersion relations by modeling simple substructures consisting of a single four-node element. To improve the calculation of dispersion relations for doubly periodic structures, a reduced model obtained by the Craig-Bampton method was first used in [15] to calculate frequencies for given wavenumbers in the case of beam grids, then in [16] to calculate wavenumbers for given frequencies in the case of more complex elastic structures. In [17–20] the reduction of boundary degrees of freedom was also taken into account, while [21] projected the mass and stiffness matrices onto a reduced set of Bloch modes. Mechanical systems incorporating damping were studied by [22] to calculate dispersion relations, while [23] studied wave propagation in highly anisotropic two-dimensional periodic textiles using WFE, focusing on reduction models to calculate dispersion relations and effective properties.

One can also be interested in obtaining the response of such structures to an external excitation. For instance, [24, 25] computed the forced response of infinite two-dimensional periodic media using WFE. In [26], two-dimensional phononic

*Corresponding author
Email address: denis.duhamel@enpc.fr (D. Duhamel)

crystals under a point force were considered. The medium is finite in one direction and infinite in the other direction. Similarly, [27, 28] computed the response of two-dimensional finite and infinite periodic structures to point harmonic and impulsive forces. For finite structures, he found the solution by a modal summation of modes with periodic boundary conditions and then extended the solution to infinite structures for points far enough from the load. In [29], the acoustic radiation of two-dimensional nearly periodic metamaterial plates was computed with 6×6 substructures by the finite element method with the Craig–Bampton reduction and interpolation strategies to reduce the computational cost. Reduction methods were also used, for instance, by [30], who computed two-dimensional periodic metamaterial structures using interior DoFs reduction by the Craig–Bampton method and an interface DoFs reduction. In [31], an approximate solution built from a linear superposition of waves was used to compute finite two-dimensional periodic structures up to 30×30 cells. More generally, [32] considered various reduction strategies for finite element modelling to compute finite periodic structures. In [33], the computation of large two-dimensional periodic structures was considered for systems described by a scalar equation.

Most of the precedent studied were made for periodic structures obtained by translation in one or two directions for respectively one-dimensional and doubly periodic structures. However, periodicity can also be observed for curves structures. For example, one directional curved waveguides have been considered using semi-analytical finite element technique (SAFE) in [34, 35] or by the WFEM with cyclic symmetry or twisted type in [36–39]. In [40] a model of a tyre was calculated by WFE using a short circumferential segment of the tyre and computation of propagation constants along the circumferential direction were obtained. The mathematically more complex case of periodic helical structures was studied by [41–43] for a single helical spring and by [44, 45] for double helical structures to calculate dispersion relations or force transmissibilities. In these cases, one-dimensional wave propagation is studied along the helix axis. Considering multi-wire helical structures, the WFEM with discrete rotational symmetry has been combined with a semi-analytical finite element approach accounting for continuous symmetry by [46]. Structures with even more complex glide, screw, and rotational symmetries are also considered by [47, 48]. In any case, the goal was to efficiently calculate the dispersion curves of different structures.

Considering more specifically the case of cylinder structures, classical work were done a long time ago by studies of vibration of simple cylinders by [49, 50]. For periodic cylinders along their axis, the case of cylinder of infinite length with periodic ribs were considered by [51] to obtain the force response and dispersion diagram. In [52] axisymmetric cylinder with periodicaxial curvature are solved by FEM and Fourrier series along the circumferential direction to obtain dispersion relations and forced response while [53] considered cylindrical shells with periodic thickness and supports. In [54] flexible risers made of ten layers were studied for deep sea oil industry while wave propagation in layered cylinder were also considered by [55] using the WFE. The forced response of infinite cylinders were studied by [56] while [57] studied wave propagation in curved metamaterial panels. Once again these studied focused mainly on the computation of dispersion relation or the response for the case of infinite structures. The study of elastic cylinders with double periodicity—namely along the axial direction and around the circumferential coordinate—but of finite sizes in these two directions can be interesting in several cases in mechanics. Such structures serve as models for fiber-reinforced composites, layered cylindrical shells, and advanced metamaterials where the geometry and material properties repeat according to two independent directions. Cylinders with two-dimensional periodicity also arise naturally in various fields of mathematics and physics, from crystallography to materials science or engineering structures. For instance, bone implants made of titanium alloy, porous and of doubly periodic cylinder shapes were considered by [58] while [59] used acrylonitrile butadiene styrene. In these studies static mechanical tests were made for obtaining the Young modulus and compressive strength of different designs of microstructure, but investigating dynamic properties would also have been interesting. In [60] doubly periodic cylindrical shell meta-structures were studied for broadband vibration reduction. In [61] cylindrical meta-structures were also proposed to study properties of tissue scaffolds for providing stability for tissue repair and growth.

The method described in this article proposes to compute the response of elastic cylinders with double periodicity for finite size cylinders. It will be based on the WFE and will use as a starting point the mass, stiffness and damping matrices of a finite element model of a rectangular substructure of the periodic medium. By imposing the wavenumber in the circumferential direction, we can numerically calculate the wavenumbers and mode shapes associated with propagation in the axial direction and thus obtain the response of the structure as a superposition of these modes. Like other WFE-type methods, the approach is limited to structures with linear behavior. In section 2, the two-dimensional waves modes will be computed. They are used in section 3 to get the response of the structure under an external load. Section 4 will present numerical examples of various complexities before the conclusion in section 5.

2. Waves in a periodic cylinder

2.1. Cylinder with two-dimensional periodicity

At its core, a cylinder with two-dimensional periodicity can be understood as a structure obtained by taking a fundamental substructure and repeating it by a rotational periodicity around its axis and also a translational periodicity along the same axis as in figure 1. Unlike simple cylinders, which exhibit periodicity in only one direction, these structures display repeating patterns in two independent directions. We seek to obtain the response of this type of structure under a load consisting of forces on its surface. To do this, we begin by obtaining a model of a substructure. Thus, the substructure is meshed with a finite element software (here Abaqus) to generate the stiffness and mass matrices of the substructure. One makes the assumption that the meshes are identical on opposite faces, on bottom and top surfaces and on left and right surfaces, see figure 2. The left and right boundaries are along the axial direction while the bottom and top boundaries are along the circumferential directions.

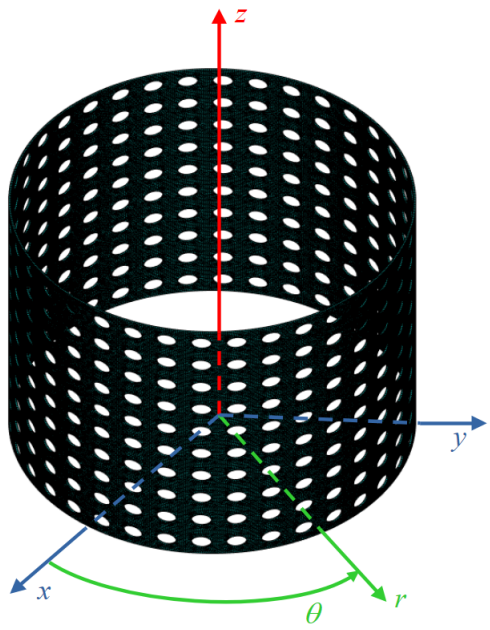

Figure 1: A cylinder with two-dimensional periodicity

2.2. Relations on boundary variables

In the aim of building wave modes, we first concentrate on the behaviour of a substructure. The discrete dynamic equation of a substructure (an elementary period) obtained from a finite element (FE) model at a circular frequency ω and for the time dependence $e^{i\omega t}$ is given by:

$$((1+\xi i)\mathbf{K}_c - \omega^2 \mathbf{M}_c)\tilde{\mathbf{q}}_c = \tilde{\mathbf{f}}_c \tag{1}$$

where $\mathbf{K}_c$ and $\mathbf{M}_c$ are the stiffness and mass matrices expressed in cartesian coordinates, respectively, and ξ is the damping coefficient, $\tilde{\mathbf{f}}_c$ is the loading vector and $\tilde{\mathbf{q}}_c$ the vector of the degrees of freedom (DoFs). Other forms of damping, such as viscous damping, would be possible as long as a dynamic stiffness matrix like $\mathbf{D}_c(\omega) = (1+\xi i)\mathbf{K}_c - \omega^2\mathbf{M}_c$ is obtained in the frequency domain. Only this dynamic stiffness matrix is needed in the following steps, and not its decomposition into a mass and static stiffness matrix. The transformation of cartesian to cylindrical coordinates is made for each node i by a rotation matrix $\mathbf{R}(\theta_i)$ such that

$$\begin{bmatrix} \tilde{q}_{ix} \\ \tilde{q}_{iy} \\ \tilde{q}_{iz} \end{bmatrix} = \begin{bmatrix} \cos\theta_i & -\sin\theta_i & 0 \\ \sin\theta_i & \cos\theta_i & 0 \\ 0 & 0 & 1 \end{bmatrix} \begin{bmatrix} \tilde{q}_{ir} \\ \tilde{q}_{i\theta} \\ \tilde{q}_{iz} \end{bmatrix} = \mathbf{R}(\theta_i) \begin{bmatrix} \tilde{q}_{ir} \\ \tilde{q}_{i\theta} \\ \tilde{q}_{iz} \end{bmatrix} \tag{2}$$

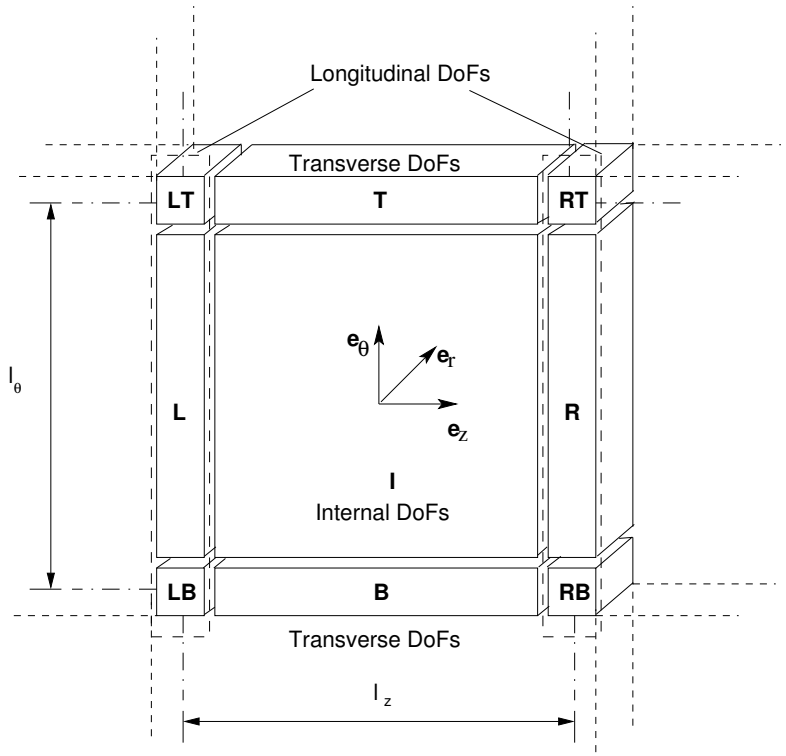

Figure 2: A substructure in the periodic medium

with θ_i the angle of node i in cylindrical coordinates. Assembling the matrices $\mathbf{R}(\theta_i)$ associated to each node i in a global block diagonal matrix $\mathbf{R}$ for all nodes, the stiffness and mass matrices are transform into their cylindrical versions $\mathbf{K}_p$ and $\mathbf{M}_p$ by

$$\begin{aligned} \mathbf{K}_p &= {}^t\mathbf{R}\mathbf{K}_c\mathbf{R} \\ \mathbf{M}_p &= {}^t\mathbf{R}\mathbf{M}_c\mathbf{R} \end{aligned} \tag{3}$$

while the displacement and load vectors are transformed by

$$\begin{aligned} \tilde{\mathbf{q}}_c &= \mathbf{R}\tilde{\mathbf{q}}_p \\ \tilde{\mathbf{f}}_p &= {}^t\mathbf{R}\tilde{\mathbf{f}}_c \end{aligned} \tag{4}$$

Introducing now the dynamic stiffness matrix $\widetilde{\mathbf{D}}_p = (1+\xi i)\mathbf{K}_p - \omega^2\mathbf{M}_p$, working only with cylindrical coordinates, decomposing the DoFs into boundary (b) and interior (i) DoFs, and assuming that there are no external forces on the interior nodes, result in the following equation:

$$\widetilde{\mathbf{D}}_p\tilde{\mathbf{q}}_p = \tilde{\mathbf{f}}_p \tag{5}$$

or

$$\begin{bmatrix} \widetilde{\mathbf{D}}_{bb} & \widetilde{\mathbf{D}}_{bi} \\ \widetilde{\mathbf{D}}_{ib} & \widetilde{\mathbf{D}}_{ii} \end{bmatrix} \begin{bmatrix} \tilde{\mathbf{q}}_b \\ \tilde{\mathbf{q}}_i \end{bmatrix} = \begin{bmatrix} \tilde{\mathbf{f}}_b \\ \mathbf{0} \end{bmatrix} \tag{6}$$

The interior DoFs can be eliminated using the second row of equation (6), which results in

$$\tilde{\mathbf{q}}_i = -\widetilde{\mathbf{D}}_{ii}^{-1}\widetilde{\mathbf{D}}_{ib}\tilde{\mathbf{q}}_b \tag{7}$$

The first row of equation (6) becomes

$$\tilde{\mathbf{f}}_b = \left(\widetilde{\mathbf{D}}_{bb} - \widetilde{\mathbf{D}}_{bi}\widetilde{\mathbf{D}}_{ii}^{-1}\widetilde{\mathbf{D}}_{ib}\right)\tilde{\mathbf{q}}_b \tag{8}$$

which can be written as

$$\tilde{\mathbf{f}}_b = \tilde{\mathbf{D}}_b\tilde{\mathbf{q}}_b \tag{9}$$

or, by dropping the b index and $\tilde{}$, in a more simplified form used in the following

$$\mathbf{f} = \mathbf{D}\mathbf{q} \tag{10}$$

It should be noted that only boundary DoFs are considered in the following. The sizes of vectors $\mathbf{q}$ and $\mathbf{f}$ equals $n_b d \times 1$ and $\mathbf{D}$ is a matrix of size $n_b d \times n_b d$ with n_b the number of nodes on the boundary of a substructure and d the number of DoFs at each node ($d = 3$ for the three-dimensional case considered here). Note that in cylindrical coordinates, the dynamic stiffness matrices are identical for all substructures.

2.3. Condensation of transverse degrees of freedom

The substructure is assumed to be meshed with an equal number of nodes on their opposite sides. The boundary DoFs are decomposed into left (L), right (R), bottom (B), top (T) DoFs and associated edges (LB), (RB), (LT) and (RT) as shown in figure 2. The global vector of boundary DoFs of size $n_b d \times 1$ is defined as

$$\mathbf{q} = \begin{pmatrix} \mathbf{q}_{LB} \\ \mathbf{q}_{L} \\ \mathbf{q}_{LT} \\ \mathbf{q}_{RB} \\ \mathbf{q}_{R} \\ \mathbf{q}_{RT} \\ \mathbf{q}_{B} \\ \mathbf{q}_{T} \end{pmatrix} \tag{11}$$

Note that $n_b = 2(n_L + n_B + 2n_{LB})d$ with n_L the number of nodes at the left boundary without its edges nodes, n_B the number of nodes at the bottom boundary without its edges nodes, n_{LB} the number of nodes at a edge and d the number of DoFs at a node. The proposed approach consists first of eliminating the DoFs of the lower and upper sides then of expressing all remaining DoFs from a reduced number of DoFs for which an eigenvalue problem will be set. First, the longitudinal DoFs vector is defined as ${}^t\mathbf{q}_l = [{}^t\mathbf{q}_{LB} \quad {}^t\mathbf{q}_{L} \quad {}^t\mathbf{q}_{LT} \quad {}^t\mathbf{q}_{RB} \quad {}^t\mathbf{q}_{R} \quad {}^t\mathbf{q}_{RT}]$ and its size is $n_l^y = 2(n_L + 2n_{LB})d$. Thus, equation (10) is rewritten as

$$\left[\begin{array}{ccc} \mathbf{D}_{ll} & \mathbf{D}_{lB} & \mathbf{D}_{lT} \\ \mathbf{D}_{Bl} & \mathbf{D}_{BB} & \mathbf{D}_{BT} \\ \mathbf{D}_{Tl} & \mathbf{D}_{TB} & \mathbf{D}_{TT} \end{array} \right] \left[\begin{array}{c} \mathbf{q}_l \\ \mathbf{q}_B \\ \mathbf{q}_T \end{array} \right] = \left[\begin{array}{c} \mathbf{f}_l \\ \mathbf{f}_B \\ \mathbf{f}_T \end{array} \right] \tag{12}$$

We are looking for solutions such that the DoFs at the bottom and top boundaries are connected by a propagation constant λ_θ along the circular direction and using the effort equilibrium at the bottom side of the cell, relations between the transverse DoFs are supposed given by

$$\begin{array}{rcl} \mathbf{q}_T & = & \lambda_\theta \mathbf{q}_B \\ \mathbf{f}_B + \frac{1}{\lambda_\theta}\mathbf{f}_T & = & 0 \end{array} \tag{13}$$

Multiplying the third row of (12) by $\frac{1}{\lambda_\theta}$, taking the sum of the second and third rows of equation (12), using conditions (13), lead to

$$\left(\mathbf{D}_{Bl} + \frac{1}{\lambda_\theta}\mathbf{D}_{Tl}\right)\mathbf{q}_l + \left(\mathbf{D}_{BB} + \mathbf{D}_{TT} + \frac{1}{\lambda_\theta}\mathbf{D}_{TB} + \lambda_\theta \mathbf{D}_{BT}\right)\mathbf{q}_B = 0 \tag{14}$$

so

$$\mathbf{q}_B = -\left(\mathbf{D}_{BB} + \mathbf{D}_{TT} + \frac{1}{\lambda_\theta}\mathbf{D}_{TB} + \lambda_\theta \mathbf{D}_{BT}\right)^{-1}\left(\mathbf{D}_{Bl} + \frac{1}{\lambda_\theta}\mathbf{D}_{Tl}\right)\mathbf{q}_l \tag{15}$$

Using (13) and (15), the first row of equation (12) becomes

$$\begin{array}{rcl} \mathbf{f}_l & = & \left[\mathbf{D}_{ll} - (\mathbf{D}_{lB} + \lambda_\theta \mathbf{D}_{lT})\left(\mathbf{D}_{BB} + \mathbf{D}_{TT} + \frac{1}{\lambda_\theta}\mathbf{D}_{TB} + \lambda_\theta \mathbf{D}_{BT}\right)^{-1} \right. \\ & & \left. \times \left(\mathbf{D}_{Bl} + \frac{1}{\lambda_\theta}\mathbf{D}_{Tl}\right)\right]\mathbf{q}_l \end{array} \tag{16}$$

which can be written as

$$\mathbf{f}_l = \mathbf{D}_l \mathbf{q}_l \tag{17}$$

The sizes of vectors $\mathbf{q}_l$ and $\mathbf{f}_l$ equals $n_l^y \times 1$ and $\mathbf{D}_l$ is a matrix of size $n_l^y \times n_l^y$. One notices that we have

$$\mathbf{D}_l(\lambda_\theta) = {}^t\mathbf{D}_l(\frac{1}{\lambda_\theta}) \tag{18}$$

2.4. One-dimensional eigenvalue problem

Introducing the propagation constants λ_z along z and λ_θ along the circular direction lead to the following relations between longitudinal DoFs

$$\begin{array}{rcl} \mathbf{q}_R &=& \lambda_z \mathbf{q}_L \\ \mathbf{q}_{RB} &=& \lambda_z \mathbf{q}_{LB} \\ \mathbf{q}_{RT} &=& \lambda_z \lambda_\theta \mathbf{q}_{LB} \\ \mathbf{q}_{LT} &=& \lambda_\theta \mathbf{q}_{LB} \end{array} \tag{19}$$

From these conditions (19), it can be seen that all components of the vector $\mathbf{q}_l$ depend on the reduced set of DoFs defined by $\mathbf{q}_r = {}^t[{}^t\mathbf{q}_{LB} \quad {}^t\mathbf{q}_L]$. This can be expressed as

$$\mathbf{q}_l = \left(\mathbf{W}_0(\lambda_\theta) + \lambda_z \mathbf{W}_1(\lambda_\theta)\right) \mathbf{q}_r \tag{20}$$

where the matrices $\mathbf{W}_0(\lambda_\theta)$ and $\mathbf{W}_1(\lambda_\theta)$ depend on the propagation constant λ_θ and are given by

$$\mathbf{W}_0(\lambda_\theta) = \begin{bmatrix} \mathbf{I}_{n_{LB}d \times n_{LB}d} & \mathbf{o}_{n_{LB}d \times n_L d} \\ \mathbf{o}_{n_L d \times n_{LB}d} & \mathbf{I}_{n_L d \times n_L d} \\ \lambda_\theta \mathbf{I}_{n_{LB}d \times n_{LB}d} & \mathbf{o}_{n_{LB}d \times n_L d} \\ \mathbf{o}_{n_{LB}d \times n_{LB}d} & \mathbf{o}_{n_{LB}d \times n_L d} \\ \mathbf{o}_{n_L d \times n_{LB}d} & \mathbf{o}_{n_L d \times n_L d} \\ \mathbf{o}_{n_{LB}d \times n_{LB}d} & \mathbf{o}_{n_{LB}d \times n_L d} \end{bmatrix} \qquad \mathbf{W}_1(\lambda_\theta) = \begin{bmatrix} \mathbf{o}_{n_{LB}d \times n_{LB}d} & \mathbf{o}_{n_{LB}d \times n_L d} \\ \mathbf{o}_{n_L d \times n_{LB}d} & \mathbf{o}_{n_L d \times n_L d} \\ \mathbf{o}_{n_{LB}d \times n_{LB}d} & \mathbf{o}_{n_{LB}d \times n_L d} \\ \mathbf{I}_{n_{LB}d \times n_{LB}d} & \mathbf{o}_{n_{LB}d \times n_L d} \\ \mathbf{o}_{n_L d \times n_{LB}d} & \mathbf{I}_{n_L d \times n_L d} \\ \lambda_\theta \mathbf{I}_{n_{LB}d \times n_{LB}d} & \mathbf{o}_{n_{LB}d \times n_L d} \end{bmatrix} \tag{21}$$

with $\mathbf{I}$ the identity matrix and $\mathbf{o}$ the null matrix. Note that the size of vector $\mathbf{q}_r$ equals $n_r^y \times 1$ with $n_r^y = (n_L + n_{LB})d$ is the number of DoFs on the left side minus the number of DoFs at the upper left edge and $\mathbf{W}_0$ and $\mathbf{W}_1$ are matrices of size $n_l^y \times n_r^y$. The equilibrium conditions between adjacent cells are given by

$$\begin{array}{rcl} \lambda_z \mathbf{f}_L + \mathbf{f}_R &=& 0 \\ \lambda_z \mathbf{f}_{LB} + \mathbf{f}_{RB} + \frac{\lambda_z}{\lambda_\theta} \mathbf{f}_{LT} + \frac{1}{\lambda_\theta} \mathbf{f}_{RT} &=& 0 \end{array} \tag{22}$$

that can be written as

$$\left(\lambda_z {}^t\mathbf{W}_0(\frac{1}{\lambda_\theta}) + {}^t\mathbf{W}_1(\frac{1}{\lambda_\theta})\right) \mathbf{f}_l = 0 \tag{23}$$

Combining (17), (20) and (23), lead to

$$\left(\lambda_z {}^t\mathbf{W}_0(\frac{1}{\lambda_\theta}) + {}^t\mathbf{W}_1(\frac{1}{\lambda_\theta})\right) \mathbf{D}_l(\lambda_\theta) \left(\mathbf{W}_0(\lambda_\theta) + \lambda_z \mathbf{W}_1(\lambda_\theta)\right) \mathbf{q}_r = 0 \tag{24}$$

that can be written as

$$\left(\mathbf{A}_{RL} + \lambda_z(\mathbf{A}_{LL} + \mathbf{A}_{RR}) + \lambda_z^2 \mathbf{A}_{LR}\right) \mathbf{q}_r = 0 \tag{25}$$

where

$$\begin{array}{rcl} \mathbf{A}_{RL}(\lambda_\theta) &=& {}^t\mathbf{W}_1(\frac{1}{\lambda_\theta}) \mathbf{D}_l(\lambda_\theta) \mathbf{W}_0(\lambda_\theta) \\ \mathbf{A}_{LL}(\lambda_\theta) &=& {}^t\mathbf{W}_0(\frac{1}{\lambda_\theta}) \mathbf{D}_l(\lambda_\theta) \mathbf{W}_0(\lambda_\theta) \\ \mathbf{A}_{RR}(\lambda_\theta) &=& {}^t\mathbf{W}_1(\frac{1}{\lambda_\theta}) \mathbf{D}_l(\lambda_\theta) \mathbf{W}_1(\lambda_\theta) \\ \mathbf{A}_{LR}(\lambda_\theta) &=& {}^t\mathbf{W}_0(\frac{1}{\lambda_\theta}) \mathbf{D}_l(\lambda_\theta) \mathbf{W}_1(\lambda_\theta) \end{array} \tag{26}$$

Note that these four matrices are of sizes $n_r^y \times n_r^y$. As we have taken a small damping, we always have $|\lambda_z| \neq 1$ and the right-going solutions must have a decreasing amplitude as we move on the right, meaning that

$$|\lambda_z^+| < 1 \tag{27}$$

The left going waves are such that

$$|\lambda_z^-| > 1 \tag{28}$$

This allows to define the eigensolutions

$$\begin{aligned}
\mathbf{\Lambda}^+(\lambda_\theta) &= [\lambda^+_{\mathtt{z}1}(\lambda_\theta)\cdots\lambda^+_{\mathtt{z}J_n^+}(\lambda_\theta)] \quad , \quad \mathbf{\Lambda}^-(\lambda_\theta) = [\lambda^-_{\mathtt{z}1}(\lambda_\theta)\cdots\lambda^-_{\mathtt{z}J_n^-}(\lambda_\theta)] \\
\mathbf{\Phi}^+_{\mathtt{q}}(\lambda_\theta) &= [\boldsymbol{\phi}^+_{\mathtt{q}1}(\lambda_\theta)\cdots\boldsymbol{\phi}^+_{\mathtt{q}J_n^+}(\lambda_\theta)] \quad , \quad \mathbf{\Phi}^-_{\mathtt{q}}(\lambda_\theta) = [\boldsymbol{\phi}^-_{\mathtt{q}1}(\lambda_\theta)\cdots\boldsymbol{\phi}^-_{\mathtt{q}J_n^-}(\lambda_\theta)] \\
\mathbf{\Phi}^+_{\mathtt{F}}(\lambda_\theta) &= [\boldsymbol{\phi}^+_{\mathtt{F}1}(\lambda_\theta)\cdots\boldsymbol{\phi}^+_{\mathtt{F}J_n^+}(\lambda_\theta)] \quad , \quad \mathbf{\Phi}^-_{\mathtt{F}}(\lambda_\theta) = [\boldsymbol{\phi}^-_{\mathtt{F}1}(\lambda_\theta)\cdots\boldsymbol{\phi}^-_{\mathtt{F}J_n^-}(\lambda_\theta)].
\end{aligned} \tag{29}$$

in which $\boldsymbol{\phi}_{\mathtt{qj}}$ is the solution of the eigenproblem (25) and $\boldsymbol{\phi}_{\mathtt{Fj}} = {}^t\left[{}^t\mathbf{f}^j_{LB} \quad {}^t\mathbf{f}^j_L\right]$ the associated force vector. Note that J_n^+ is the number of right-going waves and J_n^- is the number of left-going waves such that $J_n^+ + J_n^- = 2n_r^y = 2(n_L + n_{LB})d$ which equals two times the size of the eigenproblem (25).

2.5. Wave mode computation

To compute the wave modes, a procedure described in [62, 63] is based on the following generalized eigenproblem

$$\mathbf{N}\mathbf{w}_j = \mu_j \mathbf{L}\mathbf{w}_j \tag{30}$$

where

$$\mathbf{L} = \begin{bmatrix} \mathbf{0} & \mathbf{I}_n \\ \mathbf{A}_{\mathtt{LR}} & \mathbf{0} \end{bmatrix} \quad , \quad \mathbf{N} = \begin{bmatrix} \mathbf{A}_{\mathtt{RL}} & \mathbf{0} \\ -(\mathbf{A}_{\mathtt{LL}} + \mathbf{A}_{\mathtt{RR}}) & -\mathbf{I}_n \end{bmatrix} \tag{31}$$

and

$$\mathbf{w}_j = \begin{bmatrix} \boldsymbol{\phi}_j \\ \frac{1}{\mu_j}\mathbf{A}_{\mathtt{RL}}\boldsymbol{\phi}_j \end{bmatrix} \tag{32}$$

with $\boldsymbol{\phi}_j$ the eigenvectors of (25). Another possibility is to directly solve the quadratic eigenvalue problem (25), for instance by the polyeig function of Matlab. A procedure has been proposed in [3, 62, 63] which provides a general closed-form expression of the relations between the left-going and right-going wave shapes. In this framework, a generalized eigenproblem based on a so-called $\mathbf{S} + \mathbf{S}^{-1}$ transformation is considered. However, this procedure consider the case ${}^t\mathbf{A}_{RL} = \mathbf{A}_{LR}$ while here we have ${}^t\mathbf{A}_{RL} \neq \mathbf{A}_{LR}$ and so this procedure cannot be applied in the present case.

3. Fast solution for the two-dimensional periodic cylinder

3.1. Global system

For a cylinder, there must be a periodicity in the circumferential direction. If there are N_θ substructures in this direction, one should have $\lambda_\theta^{N_\theta} = 1$ and the propagations constants λ_θ are the N_θ roots of unity given by $\lambda_\theta = e^{2n\pi i/N_\theta}$ for $0 \leq n < N_\theta$. The forces on the global left and right boundaries in subsection p of the circumferential direction and in cylindrical coordinates can then be decomposed as, if there are N_z substructures along the axial direction,

$$\begin{aligned}
\mathbf{f}_L(p) &= \sum_{n=0}^{n=N_\theta-1} e^{i2\pi pn/N_\theta}\left(\mathbf{F}^{z+}_{Ln}\mathbf{a}^{z+}_n - \mathbf{F}^{z-}_{Rn}(\mathbf{\Lambda}^{z-}_n)^{-N_z}\mathbf{a}^{z-}_n\right) \\
\mathbf{f}_R(p) &= \sum_{n=0}^{n=N_\theta-1} e^{i2\pi pn/N_\theta}\left(-\mathbf{F}^{z+}_{Ln}(\mathbf{\Lambda}^{z+}_n)^{N_z}\mathbf{a}^{z+}_n + \mathbf{F}^{z-}_{Rn}\mathbf{a}^{z-}_n\right)
\end{aligned} \tag{33}$$

with $\mathbf{a}^{z+}_n$ and $\mathbf{a}^{z-}_n$ the amplitudes of the waves of the right-going and left-going waves along the axis respectively. One also has

$$\begin{aligned}
\mathbf{\Lambda}^{z+}_n &= diag\left(\lambda^+_{znj}\right)_{j=1\ldots J_n^+}, & \mathbf{\Lambda}^{z-}_n &= diag\left(\lambda^-_{znj}\right)_{j=1\ldots J_n^-} \\
\mathbf{F}^{z+}_{Ln} &= \left[\boldsymbol{\phi}^{z+}_{FLn1},\ldots,\boldsymbol{\phi}^{z+}_{FLnj},\ldots,\boldsymbol{\phi}^{z+}_{FLnJ_n^+}\right], & \mathbf{F}^{z-}_{Ln} &= \left[\boldsymbol{\phi}^{z-}_{FLn1},\ldots,\boldsymbol{\phi}^{z-}_{FLnj}\ldots,\boldsymbol{\phi}^{z-}_{FLnJ_n^-}\right] \\
\mathbf{F}^{z+}_{Rn} &= \left[\boldsymbol{\phi}^{z+}_{FRn1},\ldots,\boldsymbol{\phi}^{z+}_{FRnj}\ldots,\boldsymbol{\phi}^{z+}_{FRnJ_n^+}\right], & \mathbf{F}^{z-}_{Rn} &= \left[\boldsymbol{\phi}^{z-}_{FRn1},\ldots,\boldsymbol{\phi}^{z-}_{FRnj}\ldots,\boldsymbol{\phi}^{z-}_{FRnJ_n^-}\right] \\
\mathbf{a}^{z+}_n &= {}^t\left[a^{z+}_{n1},\ldots,a^{z+}_{nj},\ldots,a^{z+}_{nJ_n^+}\right], & \mathbf{a}^{z-}_n &= {}^t\left[a^{z-}_{n1},\ldots,a^{z-}_{nj},\ldots,a^{z-}_{nJ_n^-}\right]
\end{aligned} \tag{34}$$

with for instance $\mathbf{F}^{z+}_{Ln}$ the forces on the left boundary for the different right-going wave modes associated to the propagation constant $e^{2n\pi i/N_\theta}$.

3.2. Solution by FFT

Denoting by $\mathbf{f}_{Ln}$ and $\mathbf{f}_{Rn}$, the Fourier coefficients of the left and right global boundary forces, obtained by a FFT of relation (33), one has by considering each component of the Fourier series

$$\begin{pmatrix} \mathbf{F}_{Ln}^{z+} & -\mathbf{F}_{Rn}^{z-}(\mathbf{\Lambda}_n^{z-})^{-N_z} \\ -\mathbf{F}_{Ln}^{z+}(\mathbf{\Lambda}_n^{z+})^{N_z} & \mathbf{F}_{Rn}^{z-} \end{pmatrix} \begin{pmatrix} \mathbf{a}_n^{z+} \\ \mathbf{a}_n^{z-} \end{pmatrix} = \begin{pmatrix} \mathbf{f}_{Ln} \\ \mathbf{f}_{Rn} \end{pmatrix} \tag{35}$$

which can be solved easily for $0 \leq n \leq N_\theta - 1$ as these are small size systems. The displacements in the global left and right boundary sections are recovered from the analogous of relations (33) by

$$\begin{aligned} \mathbf{q}_L(p) &= \sum_{n=0}^{n=N_\theta-1} e^{i2\pi pn/N_\theta} \left(\mathbf{Q}_{Ln}^{z+}\mathbf{a}_n^{z+} + \mathbf{Q}_{Rn}^{z-}(\mathbf{\Lambda}_n^{z-})^{-N_z}\mathbf{a}_n^{z-} \right) \\ \mathbf{q}_R(p) &= \sum_{n=0}^{n=N_\theta-1} e^{i2\pi pn/N_\theta} \left(\mathbf{Q}_{Ln}^{z+}(\mathbf{\Lambda}_n^{z+})^{N_z}\mathbf{a}_n^{z+} + \mathbf{Q}_{Rn}^{z-}\mathbf{a}_n^{z-} \right) \end{aligned} \tag{36}$$

with

$$\begin{aligned} \mathbf{Q}_{Ln}^{z+} &= \left[\boldsymbol{\phi}_{qLn1}^{z+}, ..., \boldsymbol{\phi}_{qLnj}^{z+}, ..., \boldsymbol{\phi}_{qLnJ_n^+}^{z+} \right], \quad \mathbf{Q}_{Ln}^{z-} = \left[\boldsymbol{\phi}_{qLn1}^{z-}, ..., \boldsymbol{\phi}_{qLnj}^{z-} ..., \boldsymbol{\phi}_{qLnJ_n^-}^{z-} \right] \\ \mathbf{Q}_{Rn}^{z+} &= \left[\boldsymbol{\phi}_{qRn1}^{z+}, ..., \boldsymbol{\phi}_{qRnj}^{z+} ..., \boldsymbol{\phi}_{qRnJ_n^+}^{z+} \right], \quad \mathbf{Q}_{Rn}^{z-} = \left[\boldsymbol{\phi}_{qRn1}^{z-}, ..., \boldsymbol{\phi}_{qRnj}^{z-} ..., \boldsymbol{\phi}_{qRnJ_n^-}^{z-} \right] \end{aligned} \tag{37}$$

The displacements of formula (36) can be obtained directly or by FFT. The solution at internal sections can also be computed easily by formula analogous to (36).

3.3. Case of an internal load

Consider now the case where a load $\mathbf{f}^{ext}$ is applied in section N_I with $0 < N_I < N_z$ while the bottom and top surfaces are free. One has

$$\begin{aligned} \mathbf{f}_0(p) &= 0 \\ \mathbf{q}_{N_I}^+(p) &= \mathbf{q}_{N_I}^-(p) \\ \mathbf{f}_{N_I}^+(p) &= \mathbf{f}_{N_I}^-(p) + \mathbf{f}^{ext} \\ \mathbf{f}_{N_z}(p) &= 0 \end{aligned} \tag{38}$$

where for instance $\mathbf{q}_{N_I}^+(p)$ is the displacement on the right of section N_I. In term of wave amplitudes, this leads to

$$\begin{aligned} 0 &= \sum_{n=0}^{n=N_\theta-1} e^{i2\pi pn/N_\theta} \left(\mathbf{F}_{Ln}^{z+}\mathbf{a}_n^{z+} - \mathbf{F}_{Rn}^{z-}(\mathbf{\Lambda}_n^{z-})^{-N_I}\mathbf{a}_n^{z-} \right) \\ \sum_{n=0}^{n=N_\theta-1} e^{i2\pi pn/N_\theta} \left(\mathbf{Q}_{Ln}^{z+}\mathbf{b}_n^{z+} + \mathbf{Q}_{Rn}^{z-}(\mathbf{\Lambda}_n^{z-})^{N_I-N_z}\mathbf{b}_n^{z-} \right) &= \sum_{n=0}^{n=N_\theta-1} e^{i2\pi pn/N_\theta} \left(\mathbf{Q}_{Ln}^{z+}(\mathbf{\Lambda}_n^{z+})^{N_I}\mathbf{a}_n^{z+} + \mathbf{Q}_{Rn}^{z-}\mathbf{a}_n^{z-} \right) \\ \sum_{n=0}^{n=N_\theta-1} e^{i2\pi pn/N_\theta} \left(\mathbf{F}_{Ln}^{z+}\mathbf{b}_n^{z+} - \mathbf{F}_{Rn}^{z-}(\mathbf{\Lambda}_n^{z-})^{N_I-N_z}\mathbf{b}_n^{z-} \right) &= \sum_{n=0}^{n=N_\theta-1} e^{i2\pi pn/N_\theta} \left(\mathbf{F}_{Ln}^{z+}(\mathbf{\Lambda}_n^{z+})^{N_I}\mathbf{a}_n^{z+} - \mathbf{F}_{Rn}^{z-}\mathbf{a}_n^{z-} \right) + \mathbf{f}^{ext} \\ 0 &= \sum_{n=0}^{n=N_\theta-1} e^{i2\pi pn/N_\theta} \left(-\mathbf{F}_{Ln}^{z+}(\mathbf{\Lambda}_n^{z+})^{N_z-N_I}\mathbf{b}_n^{z+} + \mathbf{F}_{Rn}^{z-}\mathbf{b}_n^{z-} \right) \end{aligned} \tag{39}$$

where $\mathbf{a}_n^{z+}, \mathbf{a}_n^{z-}$ are the amplitudes of the waves in sections at the left of N_I while $\mathbf{b}_n^{z+}, \mathbf{b}_n^{z-}$ are the amplitudes on the right of N_I. The solution of this last system gives the amplitudes in both parts of the structure. Once again it can be easily found by projecting along the Fourier coefficients leading to the solutions of systems like

$$\begin{pmatrix} \mathbf{F}_{Ln}^{z+} & -\mathbf{F}_{Rn}^{z-}(\mathbf{\Lambda}_n^{z-})^{-N_I} & \mathbf{0} & \mathbf{0} \\ \mathbf{Q}_{Ln}^{z+}(\mathbf{\Lambda}_n^{z+})^{N_I} & \mathbf{Q}_{Rn}^{z-} & -\mathbf{Q}_{Ln}^{z+} & -\mathbf{Q}_{Rn}^{z-}(\mathbf{\Lambda}_n^{z-})^{N_I-N_z} \\ -\mathbf{F}_{Ln}^{z+}(\mathbf{\Lambda}_n^{z+})^{N_I} & \mathbf{F}_{Rn}^{z-} & \mathbf{F}_{Ln}^{z+} & -\mathbf{F}_{Rn}^{z-}(\mathbf{\Lambda}_n^{z-})^{N_I-N_z} \\ \mathbf{0} & \mathbf{0} & -\mathbf{F}_{Ln}^{z+}(\mathbf{\Lambda}_n^{z+})^{N_z-N_I} & \mathbf{F}_{Rn}^{z-} \end{pmatrix} \begin{pmatrix} \mathbf{a}_n^{z+} \\ \mathbf{a}_n^{z-} \\ \mathbf{b}_n^{z+} \\ \mathbf{b}_n^{z-} \end{pmatrix} = \begin{pmatrix} \mathbf{0} \\ \mathbf{0} \\ \mathbf{f}_n^{ext} \\ \mathbf{0} \end{pmatrix} \tag{40}$$

with $\mathbf{f}_n^{ext}$ the n^{th} Fourier coefficient of the external force $\mathbf{f}^{ext}$. The solution can be recovered by formula such as (36) using the $\mathbf{a}_n^{z+}, \mathbf{a}_n^{z-}$ for sections at the left of N_I and the amplitudes $\mathbf{b}_n^{z+}, \mathbf{b}_n^{z-}$ on the right of N_I.

		$N_z = 5$	$N_z = 20$	$N_z = 100$
$\Delta\theta = 1^o$	FEM	4.5	31.4	498.5
	WFE	0.7	0.7	0.9
$\Delta\theta = 2^o$	FEM	4.2	33.5	310.0
	WFE	0.3	0.4	0.4
$\Delta\theta = 5^o$	FEM	3.8	22.7	229.6
	WFE	0.4	0.3	0.5
$\Delta\theta = 10^o$	FEM	3.9	34.5	383.6
	WFE	1.1	1.2	1.8
$\Delta\theta = 20^o$	FEM	3.8	28.3	259.4
	WFE	2.5	2.7	3.4

Table 1: Comparison of computing times in seconds for the FEM and the WFE for different numbers of period N_z along the z axis and different opening angles $\Delta\theta$ of the substructure in the circumferential direction.

4. Numerical examples

4.1. Homogeneous cylinder

We consider first a thin homogeneous cylinder whose substructure is plotted in figure 3a. A basic mesh and a refined mesh are used. In this case, the substructure can be chosen as we want along the circumferential and axial directions. The external radius of the cylinder is $1m$, the thickness $1cm$ and the length of the substructure along z is $0.2m$. The cylinder is made of 20 substructures along its axis so with a total length of $4m$. The angular sectors shown in figure 3a have an opening of 10^0 so that the closed cylinder is made of 36 substructures in the circumferential direction. An example of a complete mesh is shown in figure 3b. The material is linear elastic with Young modulus $E = 70\ 10^9 Pa$, Poisson ratio $\nu = 0.3$ and density $\rho = 2700 kg/m^3$. A uniform unit pressure is applied at both ends of the cylinder. The computations are done in the case of the basic mesh for the classical FEM and for the WFE methods to allow the comparison of both methods. For the full FEM, there are 390744 DoFs, see the mesh in figure 3b. The amplitudes of displacements are plotted for the FEM and 2D WFE in figure 4 and 5 for the frequency $200Hz$ and $2000Hz$ respectively. In both cases a very good agreement is observed between the FEM and WFE computations. The computing time is $1.2s$ for the WFE and $34.5s$ for the FEM. This computing time is independent of the frequency and only depends on the mesh size. For a cylinder with the fine mesh of the right of figure 3a the results are the same as in figures 4 and 5 but the computing time is now $10.9s$ for the WFE and 212.9 for the FEM.

In a more complete way, in table 1, we compare the computing time of the FEM and WFE computation for the homogeneous cylinder with different numbers of periods along the z axis denoted N_z and for substructures with different opening angles $\Delta\theta$ in the circumferential direction. For example if $\Delta\theta = 1^o$, one has 360 substuctures in the circumferential direction. To get the total number of substructures in the whole FEM model, one has to multiply this number by N_z. The mesh density is approximately the same in all cases. From these results, we can conclude that the computation time for the WFE method depends very little on the number of substructures along the cylinder's axis, unlike the FEM method, for which the computation time increases significantly with this number of substructures. Regarding the computation time as a function of the aperture angle $\Delta\theta$, it is virtually constant for the FEM method. For the WFE method, there appears to be an optimal aperture size between 2^o and 5^o. Indeed, on the one hand, this computation time increases with the number of substructures along the circumference, but when the size of a substructure is large, it can contain a significant number of DOFS, which makes the calculation of the wave modes more difficult.This may explain why the calculation time increases for small and large values of the opening angle. Regarding memory size, table 2 gives the number of degrees of freedom and the number of non-zero coefficients for the dynamic stiffness matrices of a substructure and for the complete finite element model as a function of the opening angle and the number of substructures along the cylinder axis N_z. The mesh density is approximately constant, which explains why the values are relatively insensitive to the opening angle in the case of the FEM model but increase sharply with the number of substructures along the axis. For a substructure, the size of the model grows regularly with the opening angle but remains very small compared to the size of the complete finite element model.

4.2. Cylinder with holes

Now we consider the case of a substructure with the same dimensions and the same material as in the precedent case but with a hole of radius $5cm$ in the center of the substructure as shown in figure 6. As can be seen, two mesh densities are

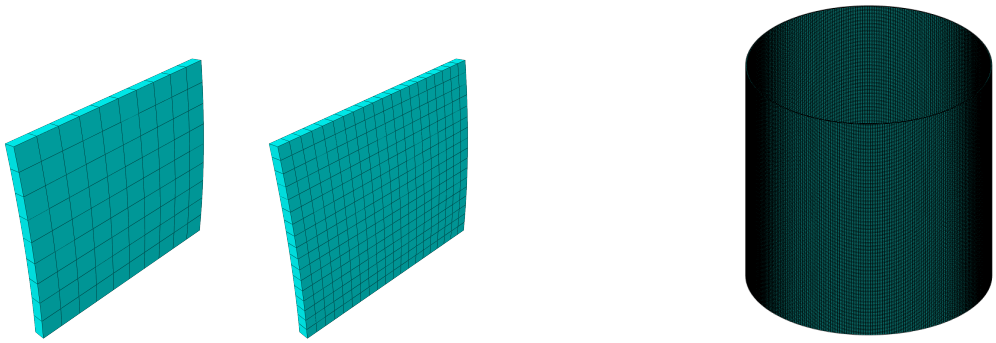

(a) Substructures of the homogeneous cylinder with normal mesh (left) and fine mesh (right).

(b) Mesh of the full homogeneous cylinder.

Figure 3: Substructure mesh and global structure mesh.

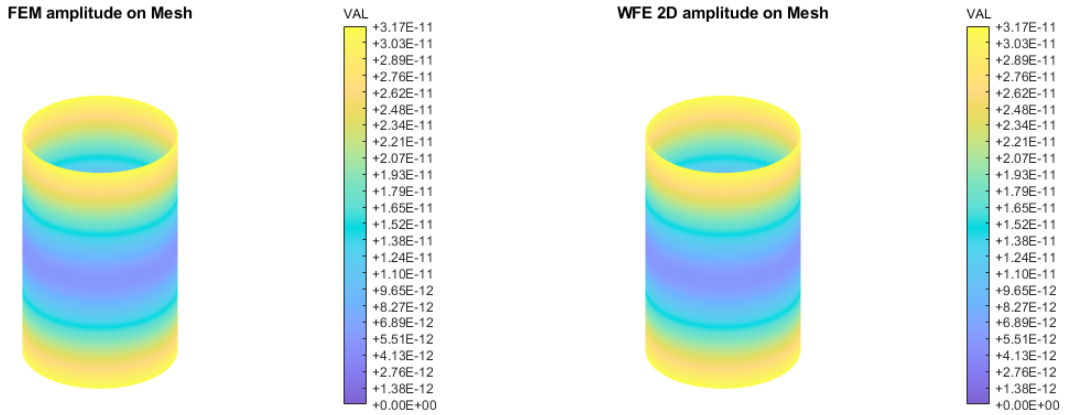

Figure 4: Amplitude of displacement for FEM (left) and 2D WFE (right) at 200Hz for the homogeneous cylinder.

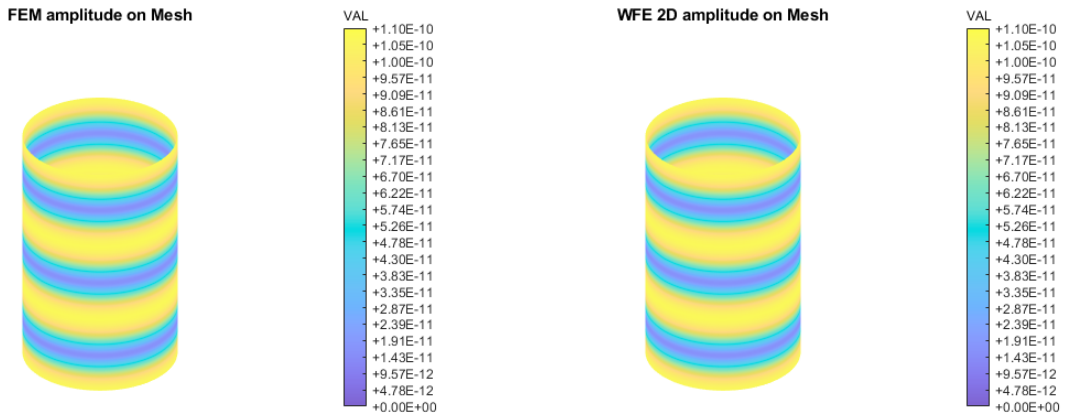

Figure 5: Amplitude of displacement for FEM (left) and 2D WFE (right) at 2000Hz for the homogeneous cylinder.

	WFE	substructure
$\Delta\theta = 1^o$	nb DoFs	132
	nnz	4.0×10^3
$\Delta\theta = 2^o$	nb DoFs	198
	nnz	7.1×10^3
$\Delta\theta = 5^o$	nb DoFs	330
	nnz	13.4×10^3
$\Delta\theta = 10^o$	nb DoFs	660
	nnz	29.3×10^3
$\Delta\theta = 20^o$	nb DoFs	1188
	nnz	53.3×10^3

	FEM	$N_z = 5$	$N_z = 20$	$N_z = 100$
$\Delta\theta = 1^o$	nb DoFs	112.6×10^3	443.8×10^3	2.2×10^6
	nnz	5.5×10^6	22.0×10^6	109.8×10^6
$\Delta\theta = 2^o$	nb DoFs	110.2×10^3	434.2×10^3	2.2×10^6
	nnz	5.6×10^6	22.1×10^6	110.4×10^6
$\Delta\theta = 5^o$	nb DoFs	88.1×10^3	347.3×10^3	1.7×10^6
	nnz	4.5×10^6	17.8×10^6	88.6×10^6
$\Delta\theta = 10^o$	nb DoFs	99.1×10^3	390.7×10^3	1.9×10^6
	nnz	5.1×10^6	20.2×10^6	101.1×10^6
$\Delta\theta = 20^o$	nb DoFs	93.6×10^3	369.0×10^3	1.8×10^6
	nnz	4.7×10^6	18.5×10^6	92.5×10^6

Table 2: Number of DoFs and number of nonzero coefficients (nnz) for a substructure on the left and total number of DoFs and number of nonzero in the global matrix for the FEM on the right.

also considered. The same computation as before is first done with a unit pressure at bottom and top surfaces of the global structure. Figures 7 and 8 present the comparison of the FEM and WFE results for the frequencies 200Hz (figure 7) and 2000Hz (figure 8). A very good agreement is observed in both cases. The computing time is $3.8s$ for WFE and $53.9s$ for FEM for the coarse mesh at $2000Hz$. For the fine mesh, the computation has not been possible by FEM due to memory limitations although the used computer has 64Go of memory. In this case, the number of Dofs is 7.3×10^6 while the number of nonzero coefficients in the dynamic stiffness matrix is 448.3×10^6 for the full FEM model. Matlab's standard solver cannot solve the problem on the computer being used due to memory issues. Iterative solvers like GMRES might be able to, but that is not the focus of this study. For the WFE, the computation was done in $94.0s$ leading to the same pictures as for the coarse mesh.

Dispersion curves for different modes orders are shown in figure 9. A mode order n is such that the variation of displacement and forces along the circumferential direction is like $\cos(n\theta)$. While mode order 0 do not show stop bands, a stop band can be seen for mode order 1 with central frequency $542.7Hz$ and width $14.2Hz$ while for mode order 2 the central frequency of the band gap is $547.6Hz$ with a width of $19.4Hz$. To observe these effects on the response of the structure, the load is now only applied at the bottom surface while all other surfaces are free. One observes the displacement in the whole structure for different frequencies and different load mode orders for a global structure with 50 substructures along its axis. In figure 10, the results are given for mode order 1. In the left, for the frequency 500Hz in a pass band, one can see a clear wave propagation on the contrary of the solution at frequency 540Hz inside a stop band where a clear attenuation can be seen along the axis of the cylinder. The same thing can be seen in figure 11 for mode order 2 where the solution is computed at 500Hz in the pass band at the left and for 550Hz in the stop band on the right. Clearly, in stop bands, only the lower part of the cylinder is vibrating while waves propagates for frequencies in pass bands.

To estimate the convergence of the WFE method, calculations were performed for the 0th order loading and the displacement at the point $(R = 1m, \theta = 0, L_z = 4m)$ on the external radius of the right boundary is determined for different mesh densities in figure 12. The calculations are done for elements of degree 1 and 2 with 5 substructures along the axis. Only the highest amplitude components are represented (real parts along x and z) versus the mesh size. We can note that the FEM and WFE results are identical, and therefore the convergence properties are also the same.

4.3. Shell meta-structures

Now we consider the case of a substructure with the same dimensions as in the precedent case but the hole now contains a resonator as in figure 13. The resonator has a radius of $2cm$ and is attached to the matrix by beams of width $1cm$. The properties of the materials are given is table 3. Dispersion curves for different modes orders are shown in figure 14. This leads to the bandgaps given in table 4.

The comparison of displacements between the FEM and WFE for frequencies 100 Hz, 135 Hz and 150 Hz are given in figure 15 for mode order two. Only the bottom surface is loaded so that we can see the transmission of vibrations for different frequencies. Once again we observe a perfect agreement between the WFE and FEM results and the effect of the bandgap at 135Hz. The computing time for each frequency is 114.1s for the FEM and 6.8s for the WFE leading to a factor 16.7 in improvement in this case. One has 61261100 non-zero coefficients in the full FEM matrix. In figure 16 we present the case where the pressure load is applied at section 10 in the middle of the cylinder. This globally leads to the

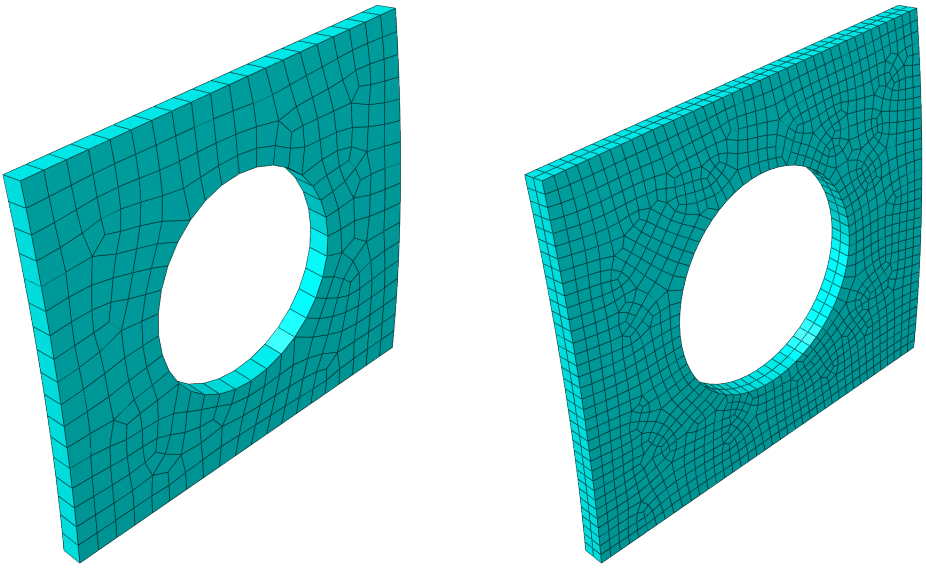

Figure 6: Substructures of the cylinder with a hole and with normal mesh (left) and fine mesh (right).

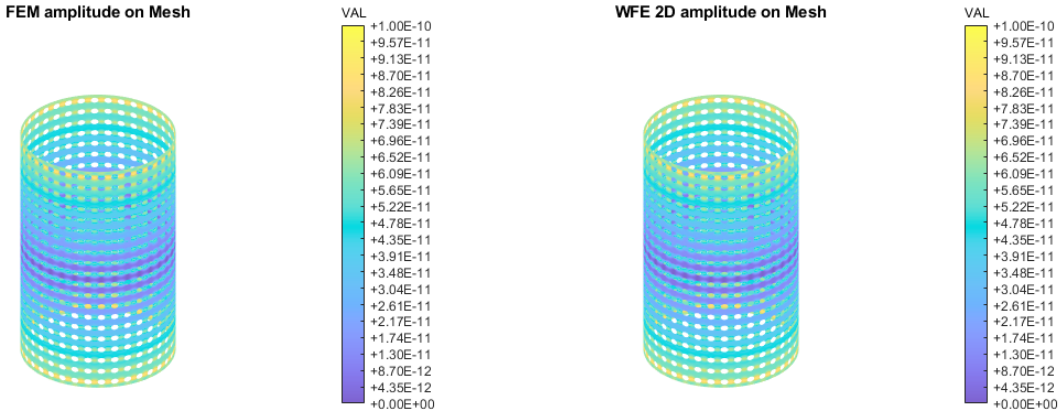

Figure 7: Amplitude of displacement for a substructure with a hole for FEM (left) and 2D WFE (right) at 200Hz.

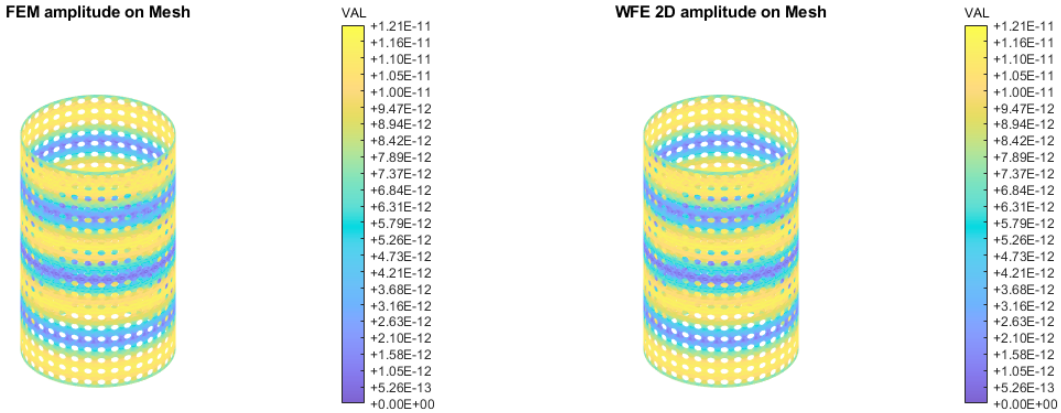

Figure 8: Amplitude of displacement for a substructure with a hole for FEM (left) and 2D WFE (right) at 2000Hz.

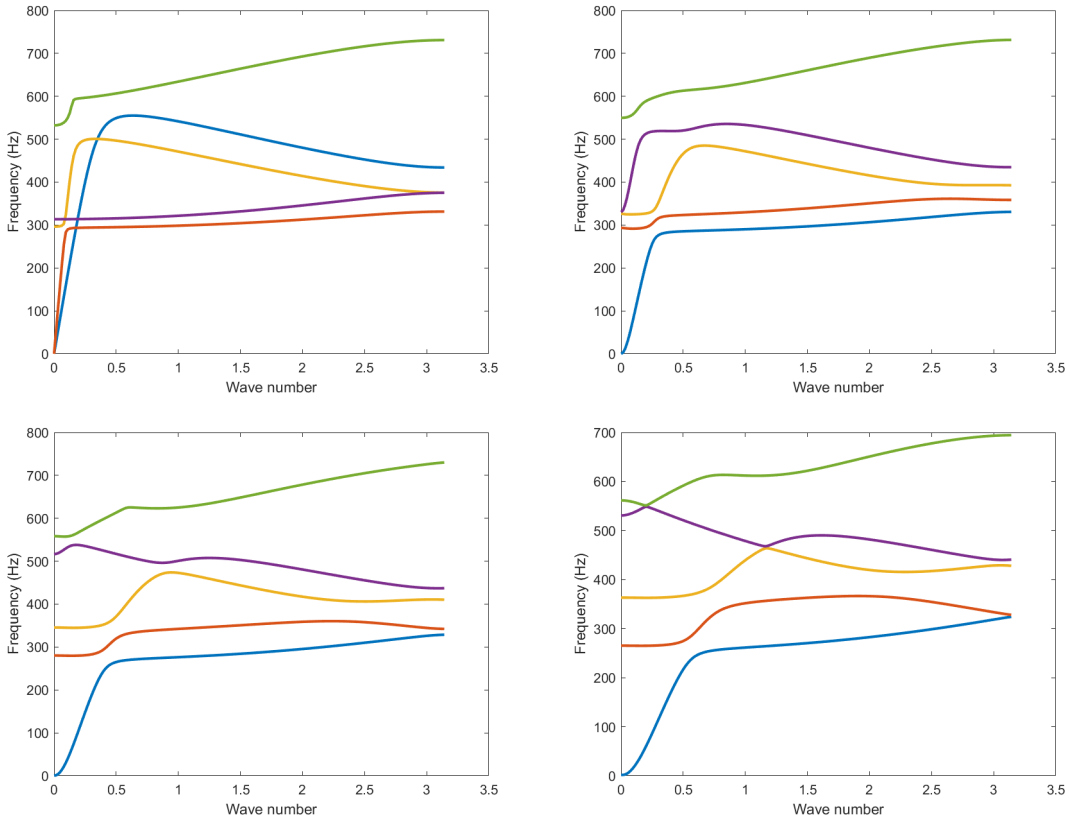

Figure 9: Dispersion curves for order 0 (left top), 1 (right top), 2 (left bottom) and 3 (right bottom).

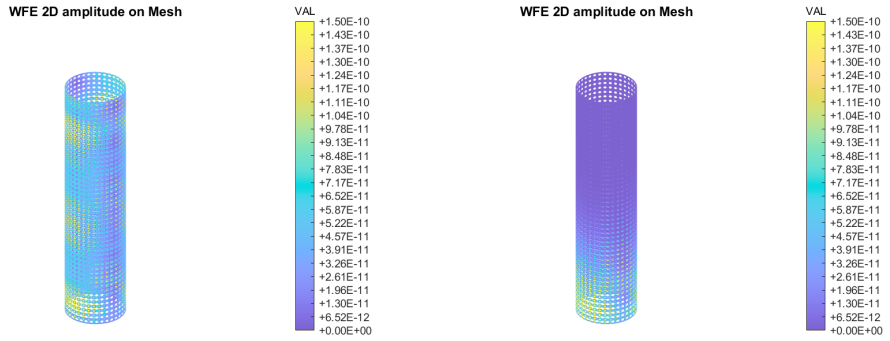

Figure 10: Amplitude of displacement for a substructure with a hole at 500Hz and load of order 1 (left) and for 540Hz (right).

Material	Young modulus (GPa)	Poisson ratio	Density (Kg/m^3)
Matrix	70.9	0.3	2700
Resonator	15	0.44	11350
Beam	0.15	0.45	930

Table 3: Properties of materials for the resonator.

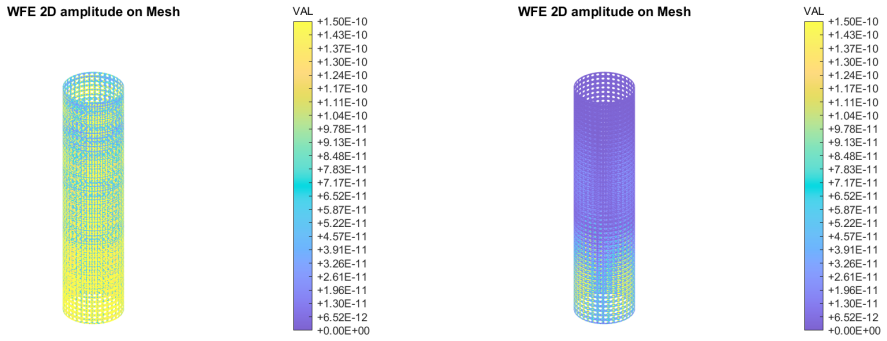

Figure 11: Amplitude of displacement for a substructure with a hole at 500Hz and load of order 2 (left) and for 550Hz and load order 2 (right).

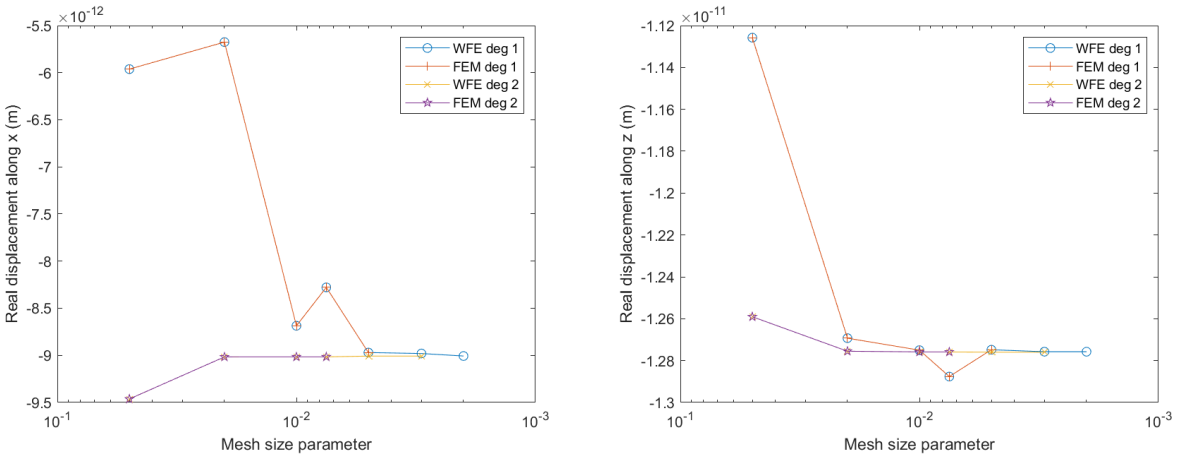

Figure 12: Displacement versus the mesh density for the FEM and WFE, real part along x on the left and real part along z on the right.

Mode order	Central frequency (Hz)	Bandwidth (Hz)
0	-	-
1	133.1	5.8
2	135.2	10.0
	413.1	4.4
	430.9	0.2
	485.5	1.6
3	136.1	11.8
	412.0	2.1
	430.9	0.1
	485.2	1.1

Table 4: Bandgap for different mode orders in the resonator case.

same comments as for the case of loads at the left and right boundaries as we can still see the effects of the pass and stop bands.

Then, we present in figure 17, the frequency response functions obtained by the WFE for loads from order 0 to order 3 on the left boundary and receivers points on the right boundary. The curves are plotted between 1 Hz and 500 Hz with a step of 1 Hz. Three points are considered at positions such that $z = 20 \times 0.2 = 4m$, on the external radius of the circle $R = 1m$ and respectively at angle 0^o (point p_1), 50^o (point p_2) and 90^o (point p_3). One can see that for order 0, the three curves are identical which was expected considering the symmetry of the load. No band of strong attenuation is seen as

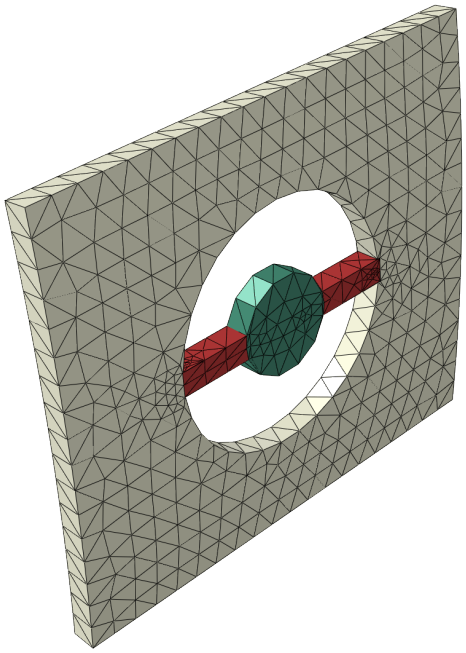

Figure 13: Substructure with a resonator.

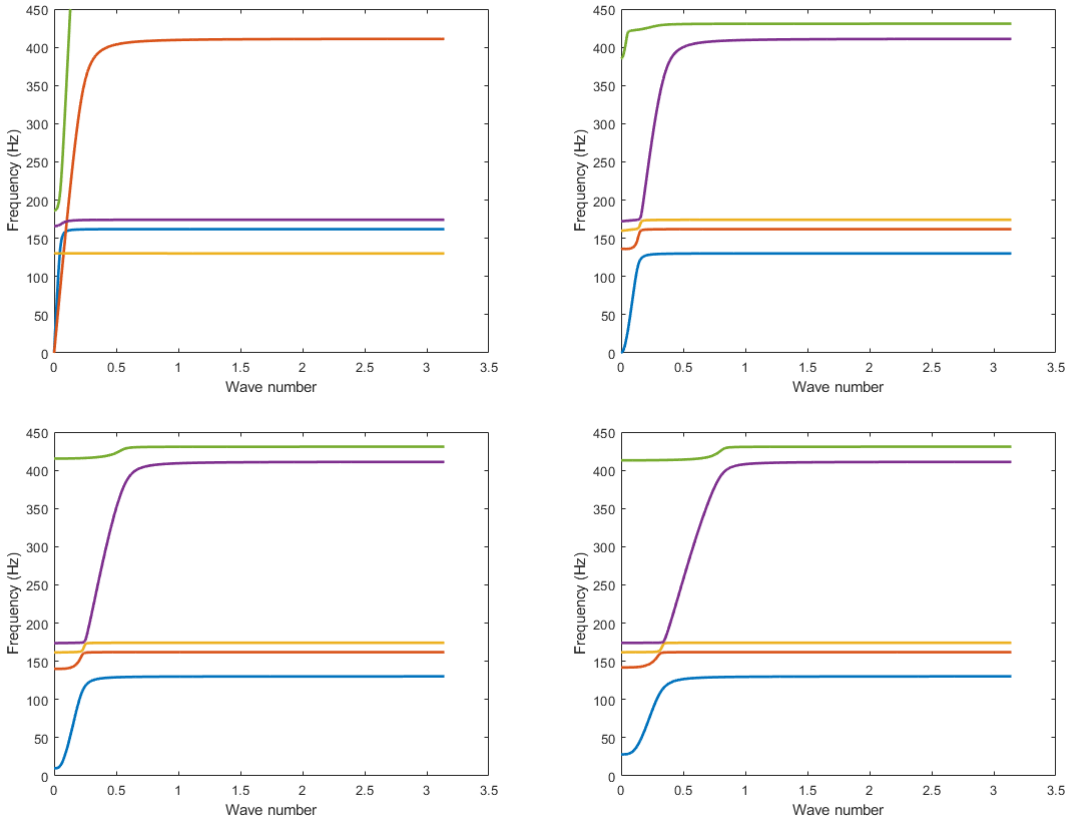

Figure 14: Dispersion curves for the resonator case and for order 0 (left top), 1 (right top), 2 (left bottom) and 3 (right bottom).

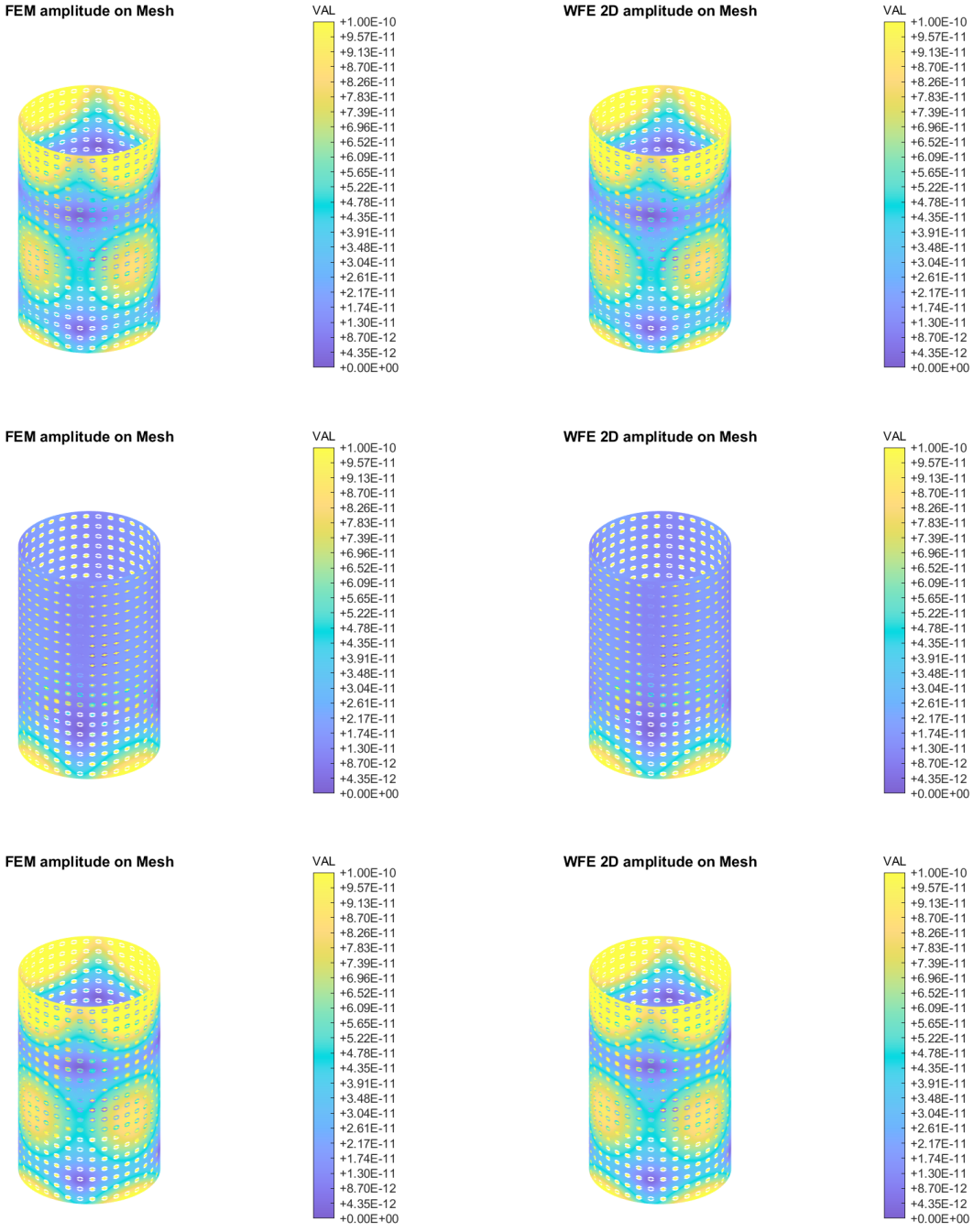

Figure 15: Amplitude of displacement for a substructure with a resonator at 100 Hz, 135 Hz and 150 Hz (from top to bottom).

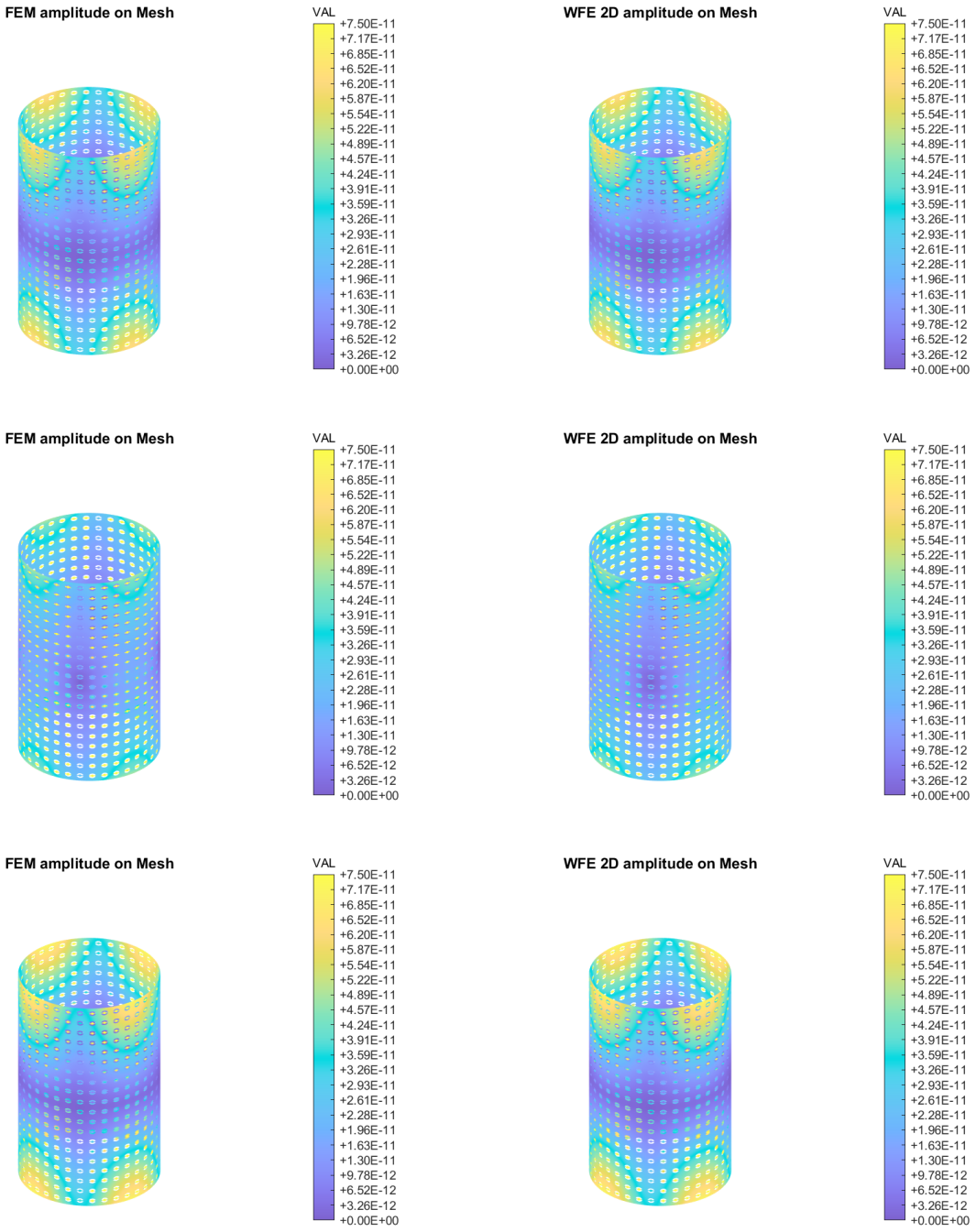

Figure 16: Amplitude of displacement for a substructure with a resonator and an internal load at 100 Hz, 135 Hz and 150 Hz (from top to bottom).

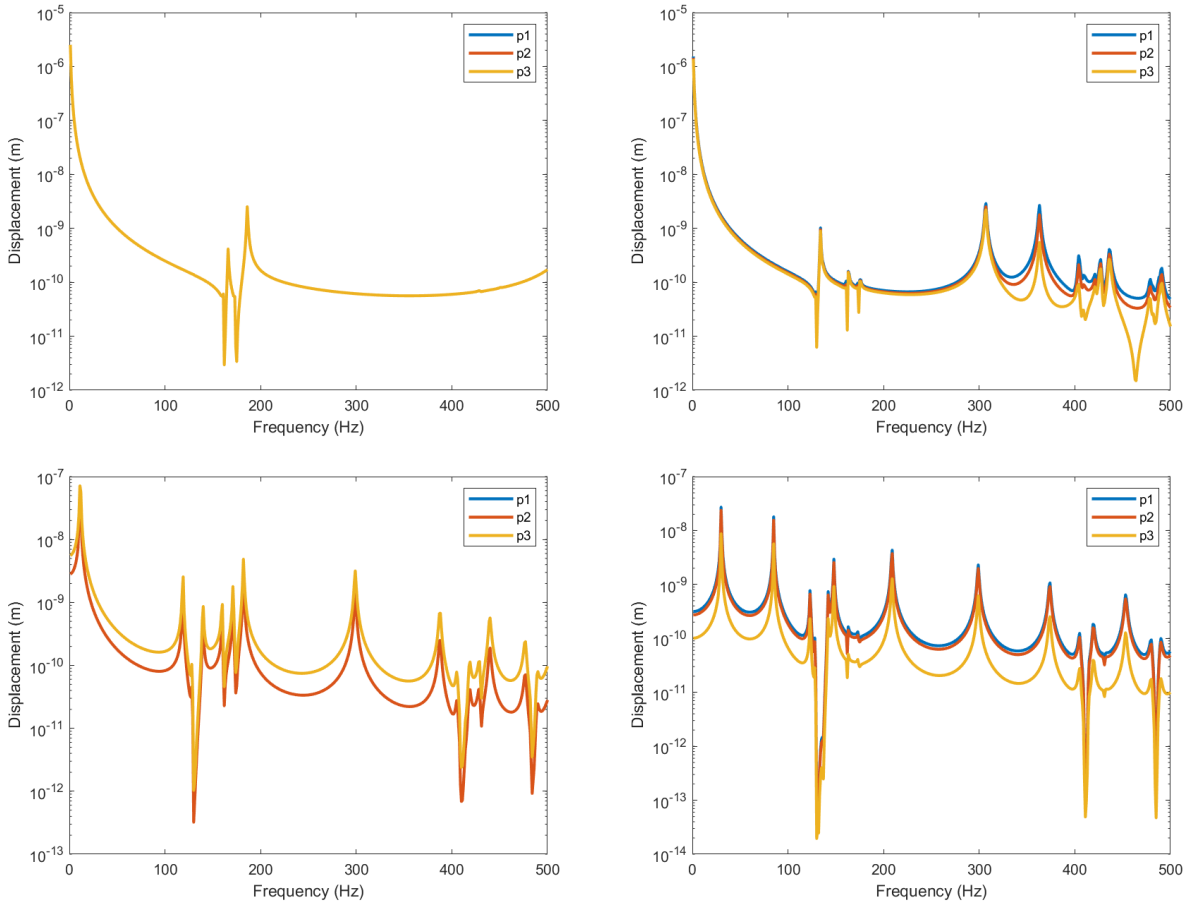

Figure 17: FRF for loads with different orders: 0 left-top, 1 right-top, 2 left-bottom, 3 right-bottom).

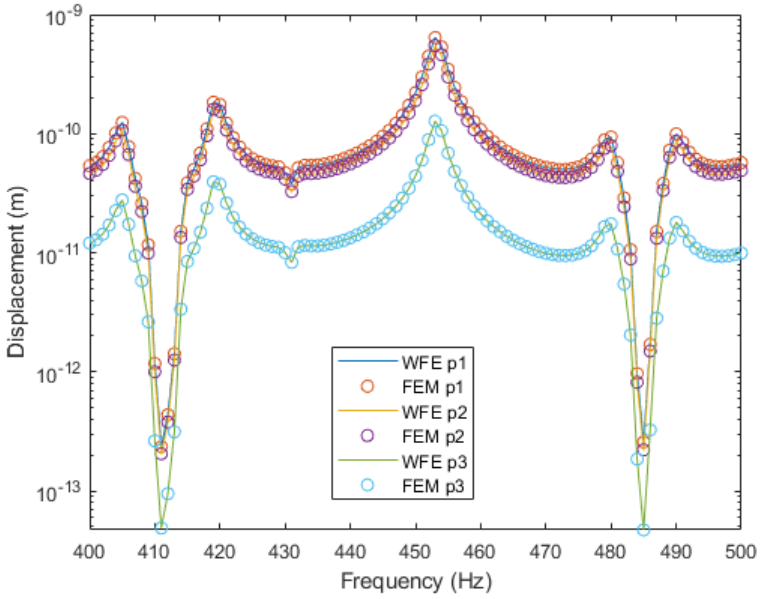

Figure 18: Comparison of the FEM and WFE FRFs for loads with order 3.

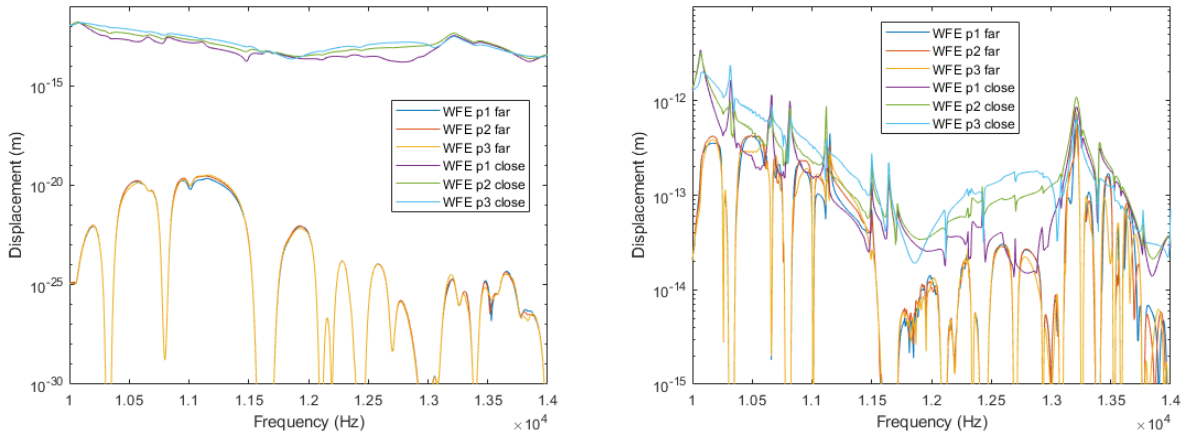

Figure 19: FRF in the high frequency range for a damping $\xi = 5 \times 10^{-3}$ on the left and $\xi = 5 \times 10^{-4}$ on the right.

there is no band gap for this load order. For the load orders 1 to 3, on the contrary, strong attenuations can be seen in the frequency bands corresponding to the band gaps of table 4. For the load order 3, a zoom is made on the frequency range $[400Hz, 500Hz]$ to compare the FEM and WFE results in figure 18. As you can see, there is a perfect agreement between the FEM and WFE results for the three points. Finally, figure 19 presents the FRF for load order 3 in the frequency range $[10kHz, 14kHz]$ for a structure with 1000 substructures along the axis. The point denoted close are taken at a distance of 5 substructures from the left while points denoted far are on the right boundary. The curves take on a regular character for the damping $\xi = 5 \times 10^{-3}$ which is the value used in the previous calculations, while a lower damping still shows resonances. With high damping, wave propagation to the right boundary is very low, whereas lower damping allows for better propagation, as expected.

5. Conclusion

By taking a Fourier series in the circumferential direction and a WFE formulation for the resulting 1D wave propagation problem, the computation of the response of the doubly periodic cylinder can be transformed into a series of problems set on only one period. Propagation constants and wave modes are obtained by an eigenvalue problem. The global solution can then be recovered by wave summation of these wave modes. This clearly leads to a big improvement over the classical finite element approach of the problem. The different examples show the displacement for different frequencies and load configurations clearly recovering the effects of pass and forbidden bands. The case of internal loads can also be considered as seen in the case of the resonator. Thus, the response of doubly periodic cylinders with a very large number of substructures can be easily obtained.

References

[1] B. Mace, D. Duhamel, M.J. Brennan, and L. Hinke. Finite element prediction of wave motion in structural waveguides. Journal of the Acoustical Society of America, 117:2835–2843, 2005.

[2] D. Duhamel, B. R. Mace, and M. J. Brennan. Finite element analysis of the vibrations of waveguides and periodic structures. Journal of Sound and Vibration, 294(1-2):205–220, 2006.

[3] J.-M. Mencik and D. Duhamel. A wave-based model reduction technique for the description of the dynamic behavior of periodic structures involving arbitrary-shaped substructures and large-sized finite element models. Finite Elements in Analysis and Design, 101:1–14, 2015.

[4] J.-M. Mencik and D. Duhamel. A wave finite element-based approach for the modeling of periodic structures with local perturbations. Finite Elements in Analysis and Design, 121:40–51, 2016.

[5] J.-M. Mencik. New advances in the forced response computation of periodic structures using the wave finite element (WFE) method. Computational Mechanics, 54(3):789–801, 2014.

[6] J.-M. Mencik. A model reduction strategy for computing the forced response of elastic waveguides using the wave finite element method. Computer Methods in Applied Mechanics and Engineering, 229-232:68–86, 2012.

[7] M. N. Ichchou, J.-M. Mencik, and W. J. Zhou. Wave finite elements for low and mid-frequency description of coupled structures with damage. Computer Methods in Applied Mechanics and Engineering, 198(15-16):1311–1326, 2009.

[8] T. Hoang, D. Duhamel, and G. Foret. Wave finite element method for waveguides and periodic structures subjected to arbitrary loads. Finite Elements in Analysis and Design, 179:103437, 2020.

[9] J. M. Renno and B. R. Mace. On the forced response of waveguides using the wave and finite element method. Journal of Sound and Vibration, 329(26):5474–5488, 2010.

[10] Y. Fan, C. W. Zhou, J. P. Laine, M. Ichchou, and L. Li. Model reduction schemes for the wave and finite element method using the free modes of a unit cell. Computers & Structures, 197:42–57, 2018.

[11] A. Abdel-Rahman. Matrix analysis of wave propagation in periodic systems. PhD thesis, University of Southampton, 1979.

[12] R. S. Langley. A note on the force boundary conditions for two-dimensional periodic structures with corner freedoms. Journal of Sound and Vibration, 167(2):377–381, 1993.

[13] A. Srikantha Phani, J. Woodhouse, and N. A. Fleck. Wave propagation in two-dimensional periodic lattices. The Journal of the Acoustical Society of America, 119(4):1995–2005, 2006.

[14] E. Manconi. Modelling wave propagation in two–dimensional structures using a wave/finite element technique. PhD thesis, University of Parma, 2008.

[15] C. W. Zhou, J. P. Lainé, M. N. Ichchou, and A. M. Zine. Multi-scale modelling for two-dimensional periodic structures using a combined mode/wave based approach. Computers & Structures, 154:145–162, 2015.

[16] A. Palermo and A. Marzani. Extended Bloch mode synthesis: Ultrafast method for the computation of complex band structures in phononic media. International Journal of Solids and Structures, 100-101:29–40, 2016.

[17] D. Krattiger and M. I. Hussein. Bloch mode synthesis: Ultrafast methodology for elastic band-structure calculations. Phys. Rev. E, 90:063306, 2014.

[18] C. Droz, C. Zhou, M. N. Ichchou, and J.-P. Lainé. A hybrid wave-mode formulation for the vibro-acoustic analysis of 2D periodic structures. Journal of Sound and Vibration, 363:285–302, 2016.

[19] D. Krattiger and M. I. Hussein. Generalized Bloch mode synthesis for accelerated calculation of elastic band structures. Journal of Computational Physics, 357:183–205, 2018.

[20] L. Van Belle, N. G. R. de Melo Filho, M. Clasing Villanueva, C. Claeys, E. Deckers, F. Naets, and W. Desmet. Fast metamaterial design optimization using reduced order unit cell modeling. In International Conference on Noise and Vibration Engineering (ISMA 2020), pages 2487–2502, Leuven, Belgium, 7-9 September, 2020.

[21] M. I. Hussein. Reduced Bloch mode expansion for periodic media band structure calculations. Proc. R. Soc. A., 465:2825–2848, 2009.

[22] M. Collet, M. Ouisse, M. Ruzzene, and M. N. Ichchou. Floquet–Bloch decomposition for the computation of dispersion of two-dimensional periodic, damped mechanical systems. International Journal of Solids and Structures, 48(20):2837–2848, 2011.

[23] V. Thierry, L. Brown, and D. Chronopoulos. Multi-scale wave propagation modelling for two-dimensional periodic textile composites. Composites Part B: Engineering, 150:144–156, 2018.

[24] D. Duhamel. Finite element computation of Green's functions. Engineering Analysis with Boundary Elements, 31(11):919–930, 2007.

[25] J. M. Renno and B. R. Mace. Calculating the forced response of two-dimensional homogeneous media using the wave and finite element method. Journal of Sound and Vibration, 330(24):5913–5927, 2011.

[26] J.-F. Lu, J. Cheng, and Q.-S. Feng. Plane wave finite element model for the 2-D phononic crystal under force loadings. European Journal of Mechanics - A/Solids, 91:104426, 2022.

[27] R. S. Langley. The response of two-dimensional periodic structures to point harmonic forcing. Journal of Sound and Vibration, 197(4):447–469, 1996.

[28] R. S. Langley. The response of two-dimensional periodic structures to impulsive point loading. Journal of Sound and Vibration, 201(2):235–253, 1997.

[29] J.-M. Mencik and M.-L. Gobert. Acoustic radiation of 2D nearly periodic metamaterial plates via finite element procedures and model reduction strategies. In International Conference on Noise and Vibration Engineering (ISMA 2022), pages 3013–3022, Leuven, Belgium, 12-14 Sep., 2022.

[30] L. Van Belle, C. Claeys, E. Deckers, and W. Desmet. Fast forced response calculations of finite metamaterial plates using a generalized Bloch mode synthesis based sub-structuring approach. In Proceedings of Euronoise, pages 1–10, Madeira, Portugal, 25-27 October, 2021.

[31] F. Qu, L. Van Belle, and E. Deckers. A unit cell wave based reduced order modelling approach for fast vibration response calculations of finite periodic metamaterial plates. In International Conference on Noise and Vibration Engineering (ISMA 2022), pages 3133–3147, Leuven, Belgium, 12-14 Sep., 2022.

[32] S. van Ophem, E. Deckers, and W. Desmet. Efficient assembly of unit cells with Krylov based model order reduction. In International Conference on Noise and Vibration Engineering (ISMA 2018), pages 445–456, Leuven, Belgium, 17-19 September, 2018.

[33] D. Duhamel. Computation of the dynamic scalar response of large two-dimensional periodic and symmetric structures by the wave finite element method. Finite Elements in Analysis and Design, 230:104096, 2024.

[34] F. Treyssède. Elastic waves in helical waveguides. Wave Motion, 45(4):457–470, 2008.

[35] F. Treyssède and L. Laguerre. Investigation of elastic modes propagating in multi-wire helical waveguides. Journal of Sound and Vibration, 329(10):1702–1716, 2010.

[36] N.G. Stephen and Y. Zhang. Eigenanalysis and continuum modelling of pre-twisted repetitive beam-like structures. International Journal of Solids and Structures, 43(13):3832–3855, 2006.

[37] J.-M. Mencik. A wave finite element approach for the analysis of periodic structures with cyclic symmetry in dynamic substructuring. Journal of Sound and Vibration, 431:441–457, 2018.

[38] J.-M. Mencik and D. Duhamel. Dynamic analysis of periodic structures and metamaterials via wave approaches and finite element procedures. In 8th International Conference on Computational Methods in Structural Dynamics and Earthquake Engineering, Athens, Greece, 28-30 June 2021.

[39] T. Hoang, D. Duhamel, G. Foret, and L.H. Tran. Wave finite element method for the dynamics of structures with cyclic symmetry. In COMPDYN 2023 9th International Conference on Computational Methods in Structural Dynamics and Earthquake Engineering, Athens, Greece, 12-14 June 2023.

[40] Y. Waki, B.R. Mace, and M.J. Brennan. Free and forced vibrations of a tyre using a wave/finite element approach. Journal of Sound and Vibration, 323(3):737–756, 2009.

[41] F. Treysède. Numerical investigation of elastic modes of propagation in helical waveguides. The Journal of the Acoustical Society of America, 121(6):3398–3408, 2007.

[42] J. M. Renno and B. R. Mace. Vibration modelling of helical springs with non-uniform ends. Journal of Sound and Vibration, 331(12):2809–2823, 2012.

[43] E. Manconi, S. Sorokin, R. Garziera, and A. Soe-Knudsen. Wave motion and stop-bands in pipes with helical characteristics using wave finite element analysis. Journal of Applied and Computational Mechanics, 4(Special Issue: Applied and Computational Issues in Structural Engineering):420–428, 2018.

[44] C. W. Zhou and F. Treyssède. Two-dimensional elastic Bloch waves in helical periodic structures. International Journal of Solids and Structures, 204-205:34–51, 2020.

[45] J. Renno, S. Sassi, and S. Gowid. Wave propagation in double helical rods. Wave Motion, 93:102446, 2020.

[46] F. Treyssède. Free and forced response of three-dimensional waveguides with rotationally symmetric cross-sections. Wave Motion, 87:75–91, 2019. Innovations in Wave Modelling II.

[47] F. Maurin. Bloch theorem with revised boundary conditions applied to glide and screw symmetric, quasi-one-dimensional structures. Wave Motion, 61:20–39, 2016.

[48] F. Maurin, C. Claeys, L. Van Belle, and W. Desmet. Bloch theorem with revised boundary conditions applied to glide, screw and rotational symmetric structures. Computer Methods in Applied Mechanics and Engineering, 318:497–513, 2017.

[49] A. W. Leissa. Vibration of Shells. NASA SP 288, 1973.

[50] M.C. Junger and D. Feit. Sound, Structures, and Their Interaction. 1986.

[51] B.-K. Jung, C. Hong, J. Ryue, W.-B. Jeong, and K.-K. Shin. Wave characteristics of a cylinder with periodic ribs. The Journal of the Acoustical Society of America, 142(5):2793–2801, 2017.

[52] A. Ghoshal, M. L. Accorsi, and M. S. Bennett. Wave propagation in circular cylindrical shells with periodic axial curvature. Wave Motion, 23(4):339–352, 1996.

[53] Dayuan Zheng, Jingtao Du, and Yang Liu. Bandgap characteristics of cylindrical shells with periodic configuration of arbitrary thickness variation and elastic supports. Journal of Vibration and Control, 31(19-20):4328–4344, 2025.

[54] J. Y. Li, Z. X. Qiu, and J. S. Ju. Numerical modeling and mechanical analysis of flexible risers. Mathematical Problems in Engineering, 2015(1):894161, 2015.

[55] E. Manconi and B. R. Mace. Wave characterization of cylindrical and curved panels using a finite element method. The Journal of the Acoustical Society of America, 125(1):154–163, 2009.

[56] J. M. Renno and B. R. Mace. Calculating the forced response of cylinders and cylindrical shells using the wave and finite element method. Journal of Sound and Vibration, 333(21):5340–5355, 2014.

[57] A. Nateghi, L. Van Belle, C. Claeys, E. Deckers, B. Pluymers, and W. Desmet. Wave propagation in locally resonant cylindrically curved metamaterial panels. International Journal of Mechanical Sciences, 127:73–90, 2017. Special Issue from International Conference on Engineering Vibration - ICoEV 2015.

[58] W.-M. Peng, Y.-F. Liu, X.-F. Jiang, X.-T. Dong, J. Jun, D. A. Baur, J.-J. Xu, H. Pan, and X. XU. Bionic mechanical design and 3D printing of novel porous Ti6Al4V implants for biomedical applications. Journal of Zhejiang University. Science. B, 20(8):647–659, 2019.

[59] M.K.A. Mohd Ariffin, S.H. Fazel, M.I.S. Ismail, S.B. Mohamed, and Z. Wahid. Mechanical properties of bone scaffold prototypes fabricated by 3D printer. Journal of Engineering Science and Technology, 13:29–38, 2018.

[60] X. An, X. Yuan, G. Sun, X. Hou, and H. Fan. Design of lattice cylindrical shell meta-structures for broadband vibration reduction and high load-bearing capacity. Thin-Walled Structures, 197:111647, 2024.

[61] X. An, P. L. Chong, I. Zohourkari, S. Roy, A. Merdji, C. L. Gnanasagaran, F. Faraji, L. K. Moey, and M. H. Yazdi. Mechanical influence of tissue scaffolding design with different geometries using finite element study. Proceedings of the Institution of Mechanical Engineers, Part H: Journal of Engineering in Medicine, 237(8):1008–1016, 2023.

[62] W-W Lin T.-M. Huang and J. Qian. Structure-preserving algorithms for palindromic quadratic eigenvalue problems arising from vibration of fast trains. SIAM Journal on Matrix Analysis and Applications, 30(4):1566–1592, 2009.

[63] W-W Lin. A new method for computing the closed-loop eigenvalues of a discrete-time algebraic Riccati equation. Linear Algebra and its Applications, 96:157–180, 1987.